

Electronic Supplementary Information (ESI)

Aliovalent Fluorine Doping and Anodization-Induced Amorphization Enable Bifunctional Catalysts for Efficient Water Splitting

Chenglin Zhong,^a Zhen Han,^a Tongtong Wang,^b Qinchao Wang,^c Zihan Shen,^a Qingwen Zhou,^a Jiaao Wang,^d Shuo Zhang,^a Xin Jin,^a Shengwen Li,^a Peng Wang,^a Daqiang Gao,^b Yongning Zhou^c and Huigang Zhang^{*a}

^aNational Laboratory of Solid State Microstructures, Collaborative Innovation Center of Advanced Microstructures, College of Engineering and Applied Sciences, and Institute of Materials Engineering Nanjing University 210093, Nanjing, China

E-mail: hgzhang@nju.edu.cn

^bKey Laboratory for Magnetism and Magnetic Materials of MOE, Key Laboratory of Special Function Materials and Structure Design of MOE, Lanzhou University 730000, Lanzhou, China

^cDepartment of Materials Science, Fudan University, Shanghai 200444, China

^dSchool of Material Science and Engineering, University of Jinan, Jinan 250022, China

Experimental Section

Synthesis of precursors: The chemicals used in the synthesis process are all analytical grade and added without further treatment. Typically, bare CC was activated by cleaning carefully with 0.5 M HNO₃ at 80 °C for 10 h, and then the CC was ultrasonically cleaned within de-ionized water and ethanol several times and directly used as the growth substrate. About 2 mmol Co(NO₃)₂·6H₂O, 1.3 mmol NH₄F, and 4 mmol urea were dissolved in 40 mL de-ionized water under vigorous stirring for 30 min to form a homogeneous suspension. After that, the as-prepared solution was transferred into a 50 ml Teflon-lined stainless-steel autoclave. For the in situ growth of the catalyst, a piece of cleaned CC (2 cm × 2 cm) was immersed into the solution. After hydrothermal treatment at 120 °C for 10 h, the precursor was coated onto the CC surface. The obtained precursor was washed with de-ionized water several times and then dried at 50 °C for 10 hours in a vacuum. In contrast, the precursor was synthesized without using NH₄F in the hydrothermal step.

Synthesis of CoO/CC and F-CoO/CC: The as-obtained precursors were separately enclosed by foil paper in a porcelain boat and placed the central positions of a tube furnace. Subsequently, the sample was heated to 400 °C with a heating rate of 10 °C min⁻¹ and hold for 2 h under a static Ar gas atmosphere. After the programmed was naturally cooled down to room temperature, and the final products of F-CoO/CC and CoO/CC were collected for further characterization. In addition, the amount of F doping in F-CoO/CC can be controlled by adjusting the holding time of heat treatment without changing any other parameters. The loading amount of F-CoO and CoO on CC were 0.248 mg cm⁻² and 0.254 mg cm⁻², respectively.

Constant current anodization: The constant current anodization process refers to the active catalyst by chronopotentiometric testing at a positive current in alkaline media. The catalyst and Pt wire were used as the work and counter electrodes, respectively. Then the catalysts were treated by applying a positive current density of 20 mA cm⁻².

Preparation of Pt/C and IrO₂ electrodes: The commercial 20 wt% Pt on Vulcan carbon (Pt/C, Johnson Matthey Corp.) was used for comparison of HER properties. First, 10 mg Pt/C catalyst was dispersed into a 1 mL of a solution of de-ionized water and ethanol (v/v = 1/1), followed by the addition of 17 μL

of Nafion solution (5%). The mixed solution was sonicated for 30 min to obtain a homogeneous catalyst ink. Second, 95 μL solution was drop-cast onto a piece of clean CC within a loading of $\sim 0.2 \text{ mg cm}^{-2}$, which was subjected to overnight solvent evaporation under ambient conditions and the Pt/C electrode obtained. The commercial IrO_2 (Adamas Reagent, Ltd.) was used for comparison of OER properties. The preparation procedure for the IrO_2 electrode was the same as that for the Pt/C electrode.

Materials Characterization: XRD patterns were collected on a Rigaku diffractometer (D/MAX 2500 V) with Cu $K\alpha$ radiation (1.5418 Å). Morphologic and EDX analyses were conducted within a Zeiss Ultra 55 field emission scanning electron microscope and a STEM (FEI Tecnai G2 20). XPS spectra were obtained using an ESCALab MKII spectrometer with Mg $K\alpha$ X-ray as the excitation source. The metal ions were quantified by inductively coupled plasma atomic emission spectroscopy (Optima 7300 DV). The Brunauer–Emmett–Teller (BET) surface area of the samples was measured using a kubo X1000 instrument via N_2 adsorption-desorption isotherms. The XAFS data were collected from the National Synchrotron Light Source II at Brookhaven National Laboratory. All measurements were conducted at room temperature under ambient pressure.

Electrochemical Measurements: The HER and OER electrochemical activities were tested using a VSP potentiostat (Bio-Logic Corp., France) with a three-electrode setup and the overall water splitting was investigated in a two-electrode system. A carbon rod and Pt wire were used as the counter electrodes in the HER and OER tests, respectively. Hg/HgO electrode was used as the reference electrode. The applied potentials were converted to the reversible hydrogen electrode (RHE) via the following equation: $E_{(\text{RHE})} = E_{(\text{Hg}/\text{HgO})} + 0.059 \times \text{pH} + 0.098 \text{ V}$. The electrolytes (1 M KOH) were deaerated using Ar (for HER) and oxygen (for OER) bubbles before the experiments. In all the experiments, the as-obtained electrodes were tailored into $1 \text{ cm} \times 1 \text{ cm}$ and directly used as the working electrodes for the electrochemical tests.

The linear sweep voltammetry (LSV) tests were conducted at a scan rate of 2 mV s^{-1} . The working electrodes were scanned for several times until the signals were stabilized. It should be noted that the obtained LSV curves were corrected for ohmic drop obtained via impedance measurements and all potential values presented in this work were referenced to RHE unless indicated otherwise. EIS measurements were performed by using an AC amplitude of 10 mV in a frequency range from 100 kHz to 100 mHz. The Tafel slopes were calculated according to the Tafel equation $\eta = b \cdot \log(j/j_0)$, where η , b , j , and j_0 represent the overpotential, Tafel slope, current density, and exchange current density,

respectively. The stability measurements were performed using chronopotentiometric measurements or potential cycling with a sweep rate of 100 mV s⁻¹, the final LSV curves were recorded at a scan rate of 2 mV s⁻¹ again.

Calculation of the double-layer capacitance (C_{dl}). The C_{dl} was used to determine the ECSA according to the reference.¹ To measure the C_{dl}, the potential was scanned between 0.12 and 0.22 V (vs. RHE) for HER and 0.98 and 1.08 V (vs. RHE) for OER at varied scan rates (10, 20, 50, 100, and 200 mV s⁻¹). This potential range was selected for the capacitance measurements because no obvious faradaic reactions can be observed in this region for any of the electrodes. The current density differences (*J_a-J_c*) were plotted as a function of the CV scan rate. The linear slope is equivalent to twice the C_{dl}, which is proportional to the ECSA of the electrode.

Calculation of the TOF. To calculate the active surface-site density and per-site TOF of F-CoO/CC and CoO/CC for HER, we adopted the method applied by Jaramillo and co-workers.²⁻⁴ The per-site TOF was calculated as follows:

$$\text{TOF} = \frac{\text{\#total hydrogen turnovers/cm}^2 \text{ geometric area}}{\text{\#surface sites/cm}^2 \text{ geometric area}}$$

The total number of hydrogen turnovers (#H₂) was calculated from the current density according to the

$$\text{\#H}_2 = \left(\frac{\text{mA}}{\text{cm}^2} \right) \left(\frac{1 \text{ C s}^{-1}}{1000 \text{ mA}} \right) \left(\frac{1 \text{ mol e}^{-1}}{96485.3 \text{ C}} \right) \left(\frac{1 \text{ mol H}_2}{2 \text{ mol e}^{-1}} \right) \left(\frac{6.022 \times 10^{23} \text{ H}_2 \text{ molecules}}{1 \text{ mol H}_2} \right)$$

following formula:

$$= 3.12 \times 10^{15} \frac{\text{H}_2/\text{s}}{\text{cm}^2} \text{ per } \frac{\text{mA}}{\text{cm}^2}$$

The number of active sites per real surface area is calculated from the following formula⁵:

$$\text{No. of active sites per real surface area} = \left(\frac{\text{No. of atoms per unit cell}}{\text{Volume per unit cell}} \right)^{2/3}$$

We calculated the active sites per real surface area of F-CoO is approximately 2.203×10¹⁵ atoms cm⁻². The real surface area is calculated from the BET specific surface area (Surface_{BET}). With the number of sites, we can calculate the TOFs. Therefore, the TOF per site at an overpotential was calculated as follows:^{6,7}

$$TOF = \frac{\left(3.12 \times 10^{15} \frac{\text{H}_2/\text{s}}{\text{cm}^2} \text{per} \frac{\text{mA}}{\text{cm}^2}\right) \times |\text{current density}|}{\text{No. of active sites per real surface area} \times \text{Surface}_{BET} \times \text{mass}}$$

DFT Computational. The electronic structures were studied using the Vienna Ab initio Simulation Package (VASP) with the projector augmented wave (PAW) method.⁸⁻¹⁰ The generalized gradient approximation functional with the revised Perdew–Burke–Ernzerhof formulation was adopted to describe the exchange–correlation interaction among electrons.¹¹ An energy cutoff of 500 eV was used for the plane wave expansion.¹² A semi-empirical van der waals (vdW) correction (optB86b-vdW) for the dispersion interactions was considered.^{13, 14} Slabs with about 10-Å thickness and a 16-Å vacuum layer along the *z*-direction were used to model the surface. The Brillouin zone was sampled with a size-dependent Monkhorst–Pack *k*-point mesh (5×5×5 and 3×5×1) for the geometric optimizations of the bulk and the slab surface of CoO, respectively. The convergence threshold was set as 10⁻⁵ eV per unit cell in energy and 0.01 eV/Å per atom in force. The electron charge transfer was performed using a Bader charge analysis.¹⁵ CI-NEB was applied to compute the decomposition barriers of H₂O molecular to obtain the minimum energy path between the given initial and final positions.¹⁶

The HER activity of an electrocatalyst is correlated to the free energy change (ΔG_{H^*}) of adsorbing a single H atom to the catalyst surface. The ΔG_{H^*} has been considered an effective descriptor for evaluating the HER activity, which is defined as:¹⁷

$$\Delta G_{\text{H}^*} = \Delta E_{\text{H}^*} + \Delta \text{ZPE} - T\Delta S$$

where ΔE_{H^*} is the binding energy of H atoms on adsorption sites. ΔZPE is the zero-point energy change of H*, which is defined as $\Delta \text{ZPE} = \text{ZPE}_{\text{H}^*} - 1/2 \text{ZPE}_{\text{H}_2}$, where $\text{ZPE}_{\text{H}_2} = 0.230$ eV. $T\Delta S$ is the entropy change of H*, which is -0.20 eV at 298 K and 1 atm according to the references.^{18, 19}

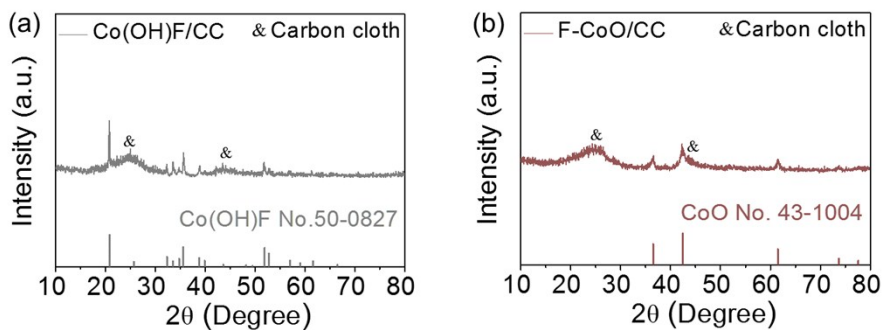


Fig. S1 The XRD patterns of (a) Co(OH)F/CC precursor and (b) F-CoO/CC.

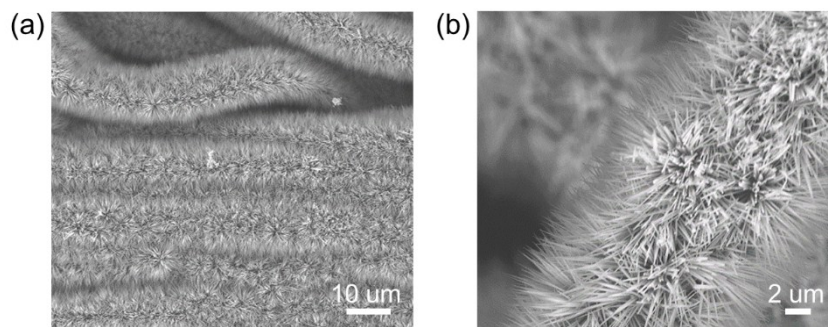


Fig. S2 (a,b) SEM images of Co(OH)F/CC precursor at two magnifications.

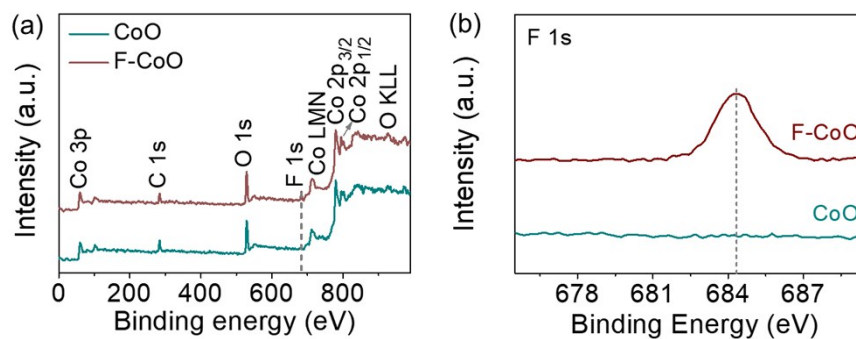


Fig. S3 The XPS analysis of (a) survey scan and (b) F 1s spectra of CoO and F-CoO nanowire.

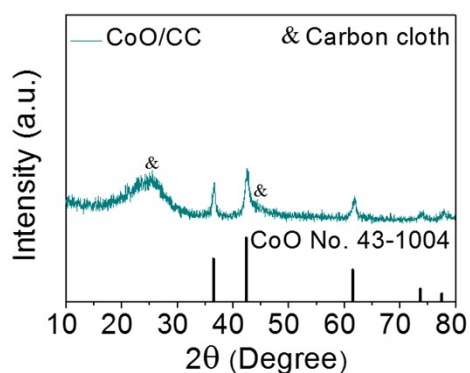


Fig. S4 The XRD pattern of the CoO/CC.

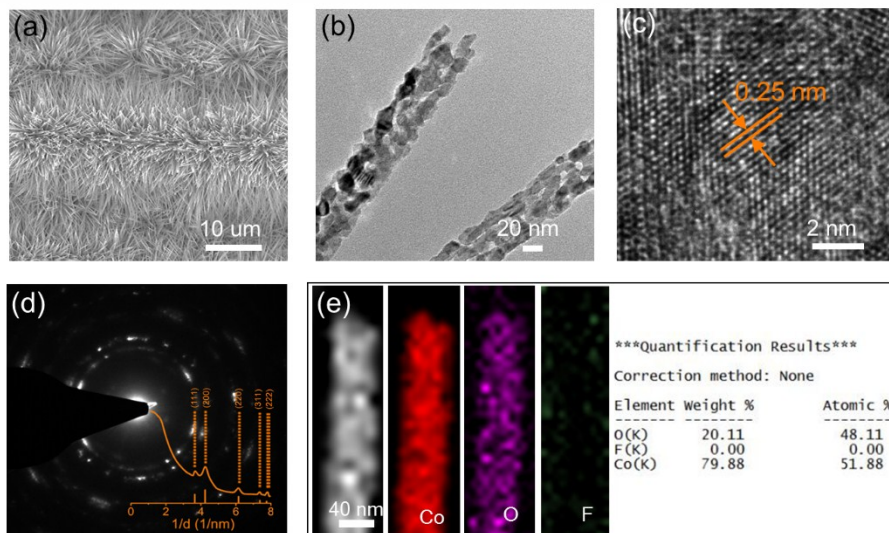


Fig. S5 (a) The SEM images of CoO/CC. (b) The TEM images, (c) The HRTEM image, (d) The SAED pattern and the rotational averaging profile of CoO nanowires. (e) EDX elemental mapping and quantification results of CoO nanowires.

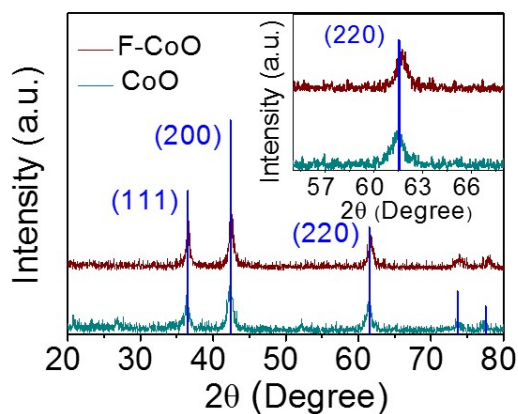


Fig. S6 The XRD patterns of F-CoO and CoO powders without CC.

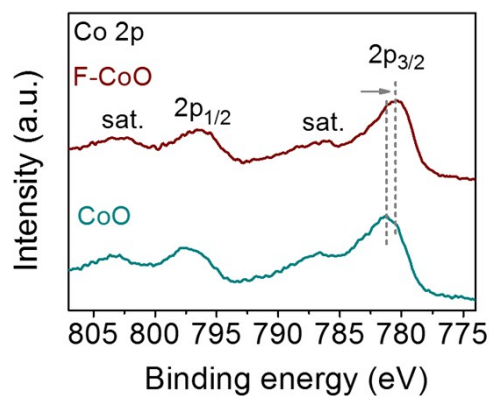


Fig. S7 XPS spectra of Co 2p signals of CoO and F-CoO nanowires.

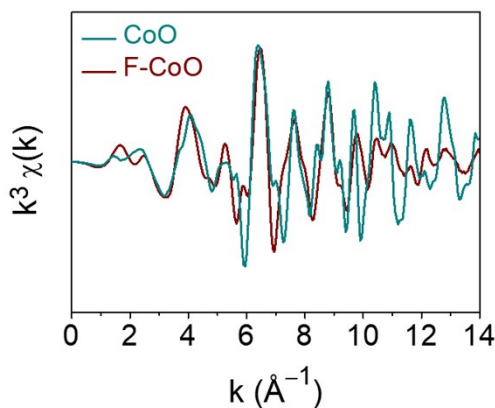


Fig. S8 The Co K-edge EXAFS oscillation function.

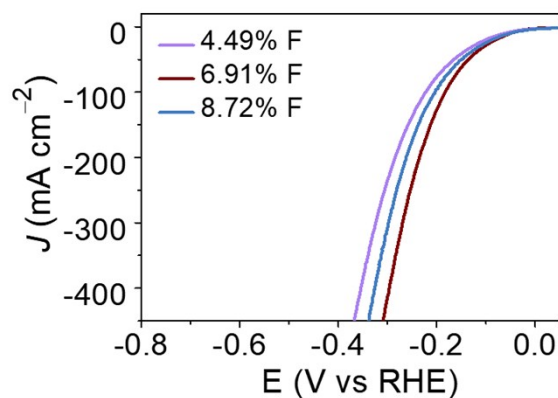


Fig. S9 The LSV curves of F-CoO/CC with different F content. The F doping content was tuned by adjusting the holding time of heat treatment (1 h, 2 h, and 3 h for 8.72 at% F, 6.91 at% F, and 4.49 at% F respectively) without changing any other parameters. As the holding time increases, the amount of F decreases. The F doping contents in these samples were measured by XPS (Table S1).

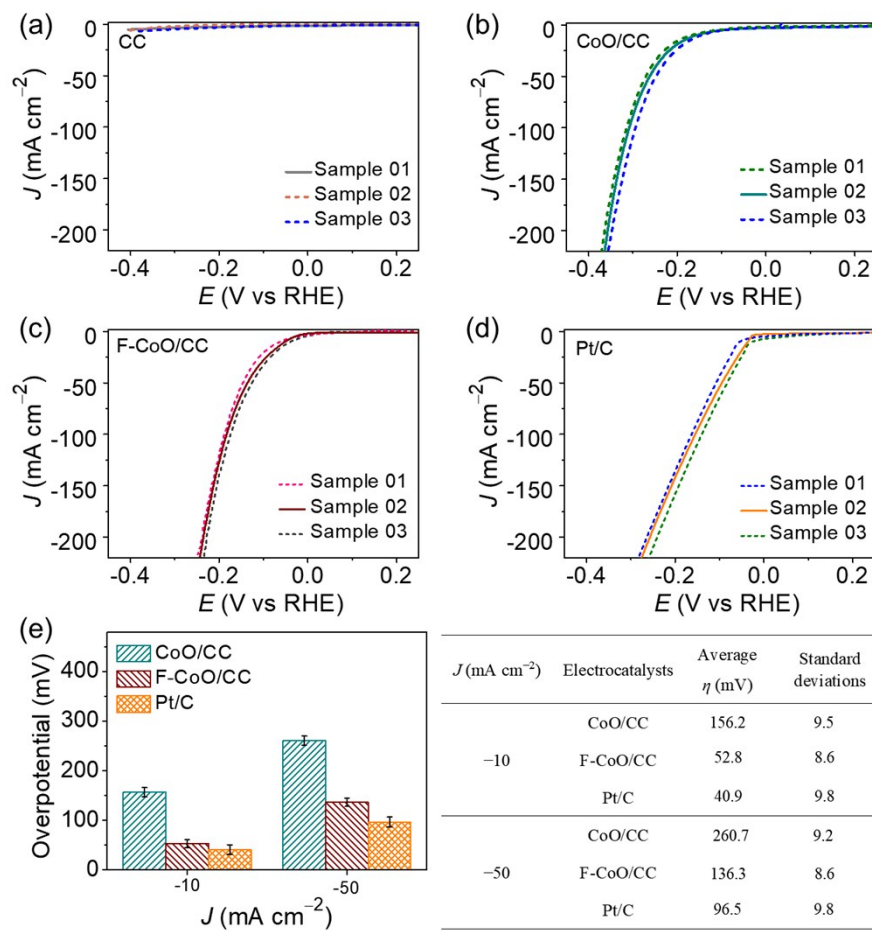


Fig. S10 LSV curves of different (a) CC samples, (b) CoO/CC samples, (c) F-CoO/CC samples, and (d) Pt/C samples for HER. (e) The corresponding average overpotentials of CoO/CC, F-CoO/CC, and Pt/C samples at -10 and -50 mA cm⁻² current density. The error bars represent the standard deviations. The HER performance of these electrocatalysts is reproducible.

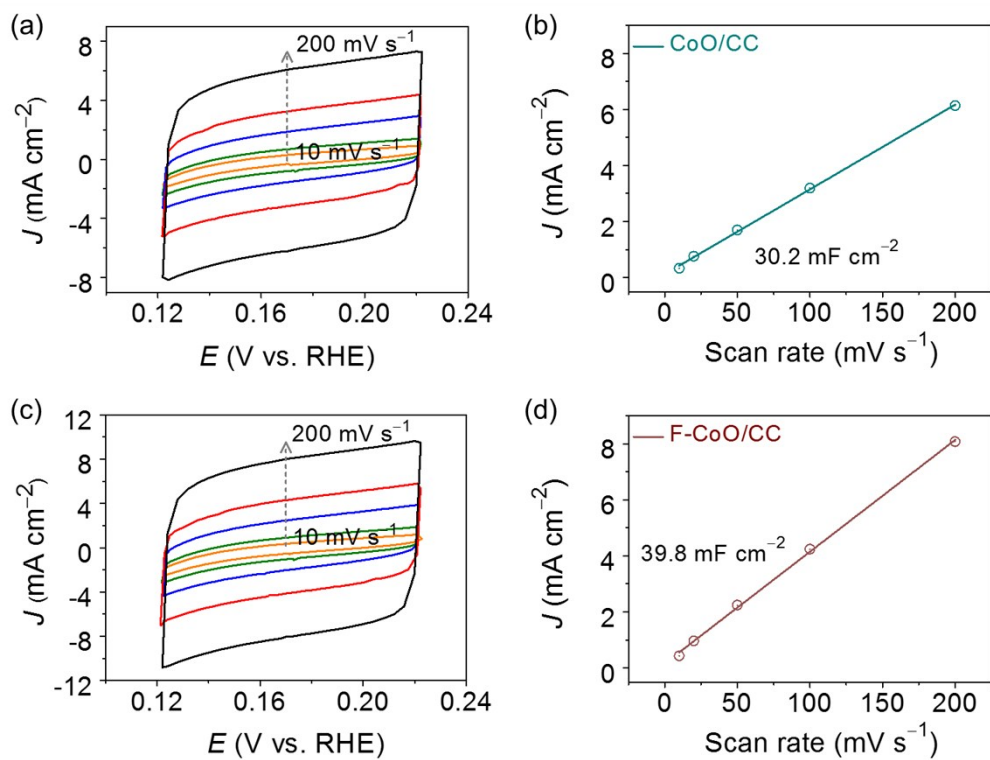


Fig. S11 CV curves and linear fitting curves of the capacitive currents for (a,b) CoO/CC and (c,d) F-CoO/CC between 0.12 and 0.22 V at 10, 20, 50, 100, and 200 mV s^{-1} .

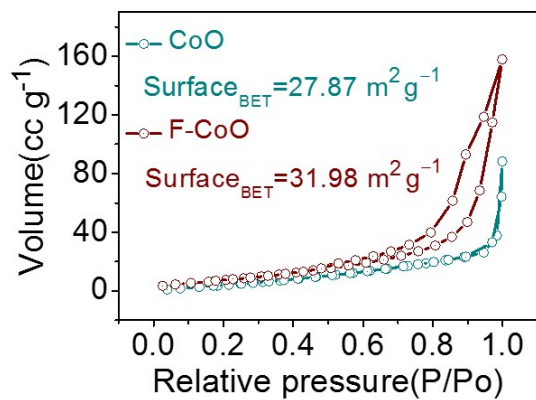


Fig. S12 N_2 adsorption/desorption isotherms of CoO and F-CoO.

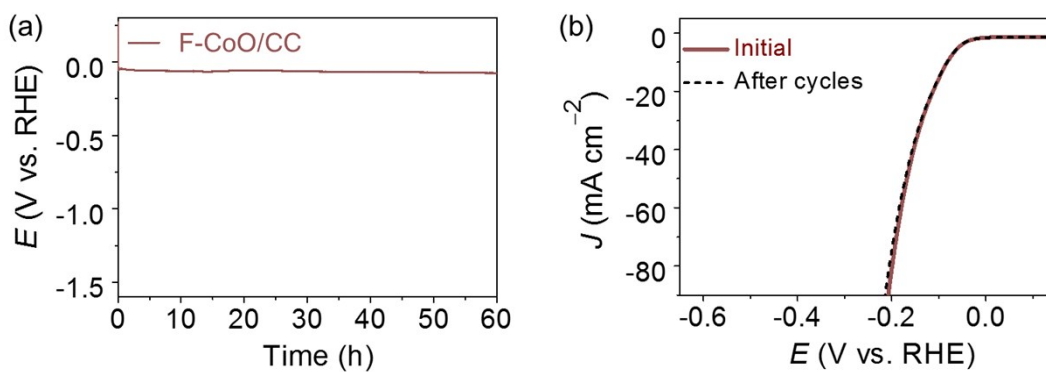


Fig. S13 (a) Chronopotentiometry curves of F-CoO/CC at a current density of -10 mA cm^{-2} for 60 h.
 (b) LSV curves of F-CoO/CC initially and after 3000 cycles.

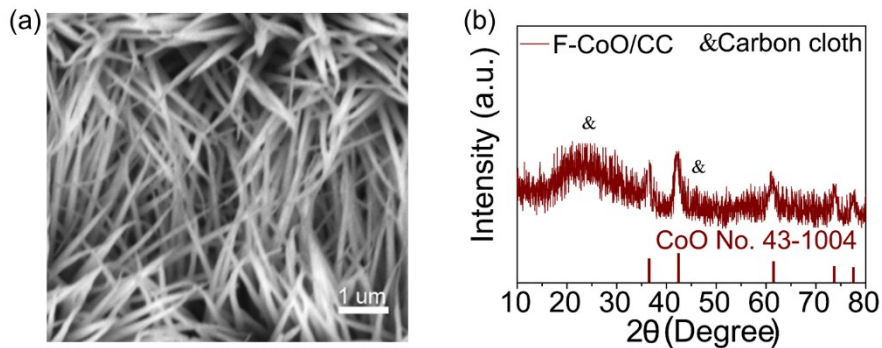


Fig. S14 (a) The SEM image and (b) XRD pattern of F-CoO/CC after the stability of HER testing.

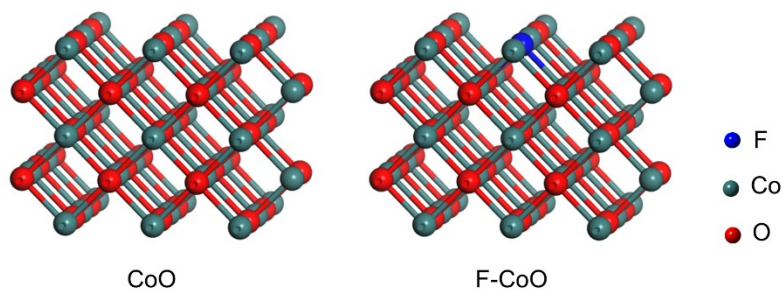


Fig. S15 Supercell models of CoO and F-CoO (110) surfaces for hydrogen (H^*) adsorption.

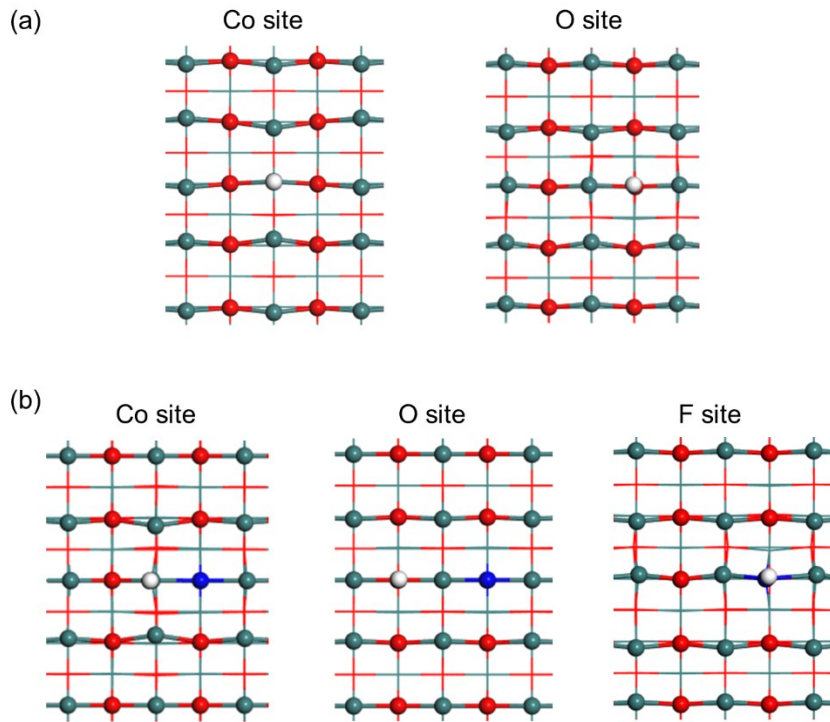


Fig. S16 The geometric configurations of H adsorption onto the (110) surfaces. (a) CoO, (b) F-CoO.

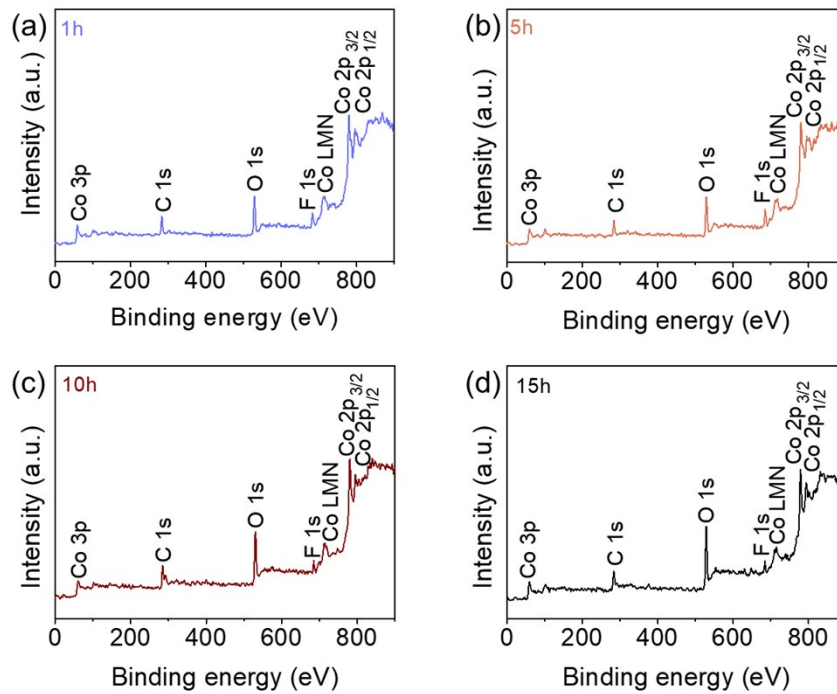


Fig. S17 The survey scan of constant current anodization F-CoO/CC for 1h, 5 h, 10 h, and 15 h.

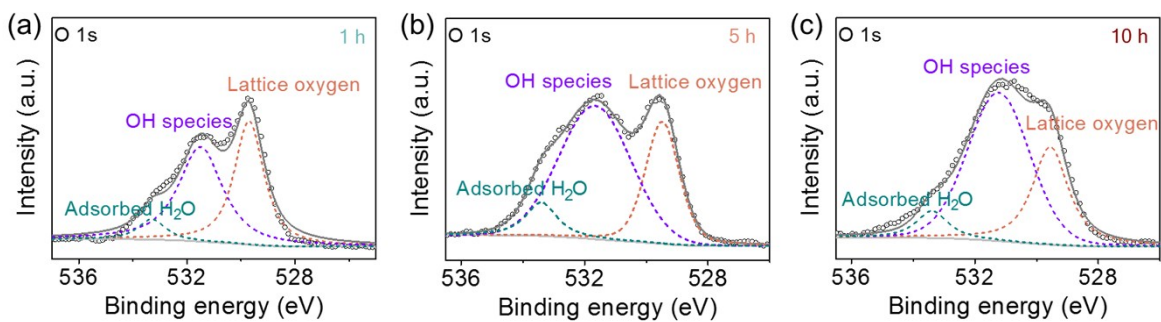


Fig. S18 (a-c) O 1s spectra of constant current anodization F-CoO/CC for 1 h (a), 5 h (b), and 10 h (c).

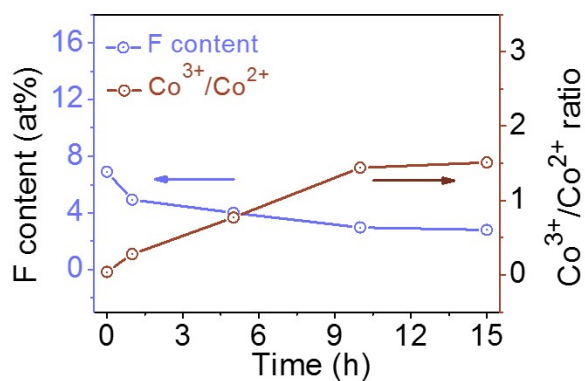


Fig. S19 The F content and Co³⁺/Co²⁺ ratio in F-CoO/CC with the constant current anodization.

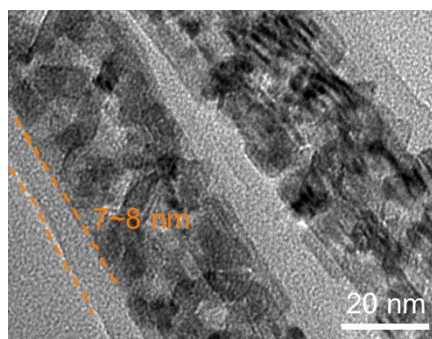


Fig. S20 TEM images of constant current anodization F-CoO/CC for 15 h.

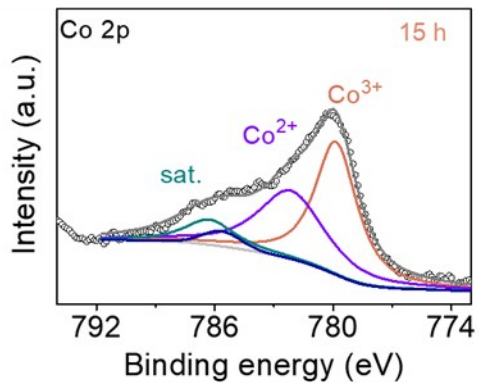


Fig. S21 Co 2p spectra of constant current anodization F-CoO/CC for 15 h.

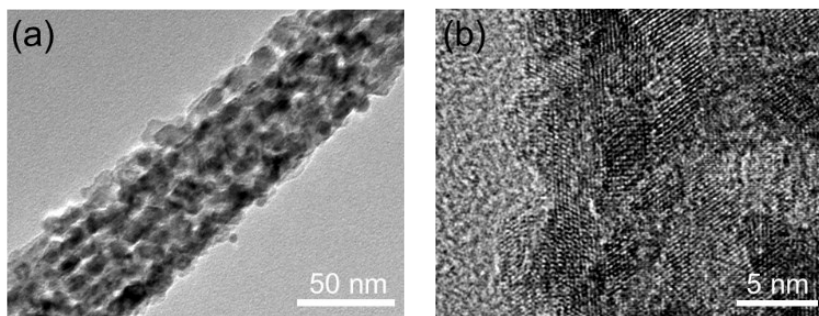


Fig. S22 TEM (a) and HRTEM (b) images of the CoO after constant current anodization for 10 h.

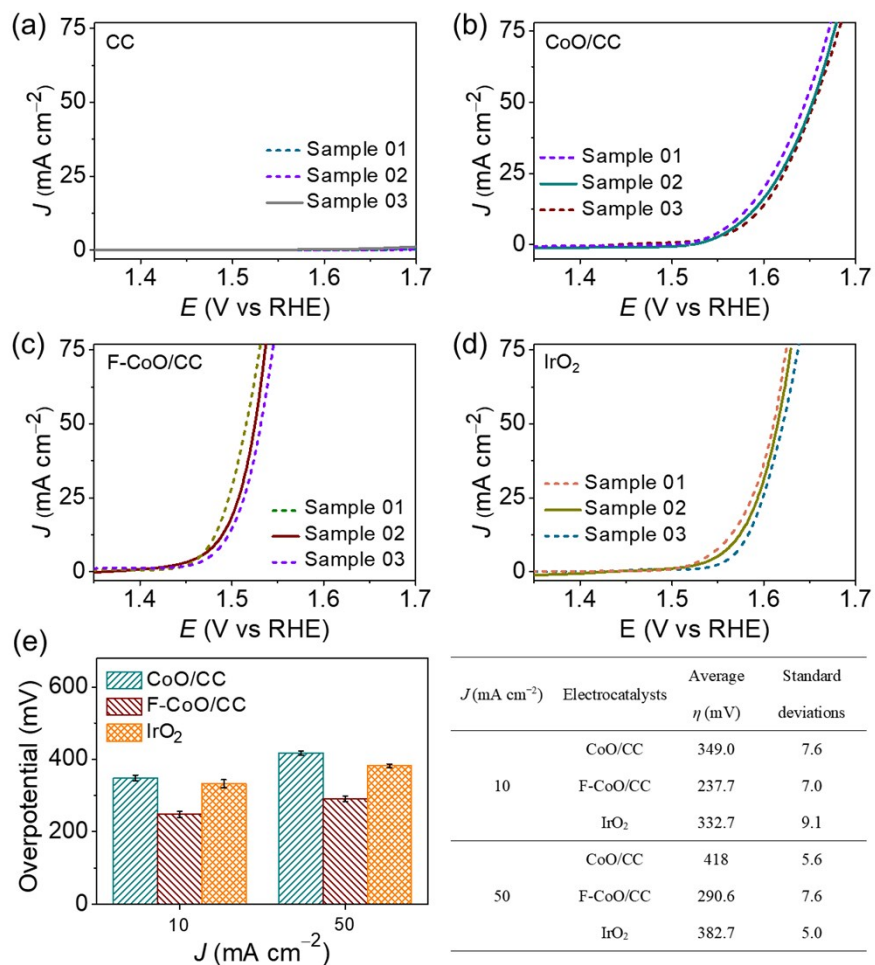


Fig. S23 LSV curves of different (a) CC samples, (b) CoO/CC samples, (c) activated F-CoO/CC samples, and (d) IrO₂ samples for OER. (e) The corresponding average overpotentials of CoO/CC, F-CoO/CC, and Pt/C samples at 10 and 50 mA cm⁻² current density. The error bars represent the standard deviations. The OER performance of these electrocatalysts is reproducible.

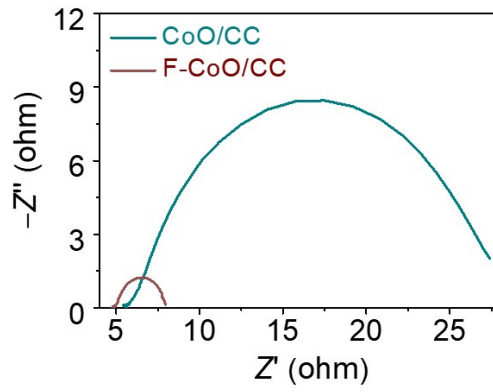


Fig. S24 Nyquist plots. (Z' and Z'' are the real and imaginary parts of impedance, respectively).

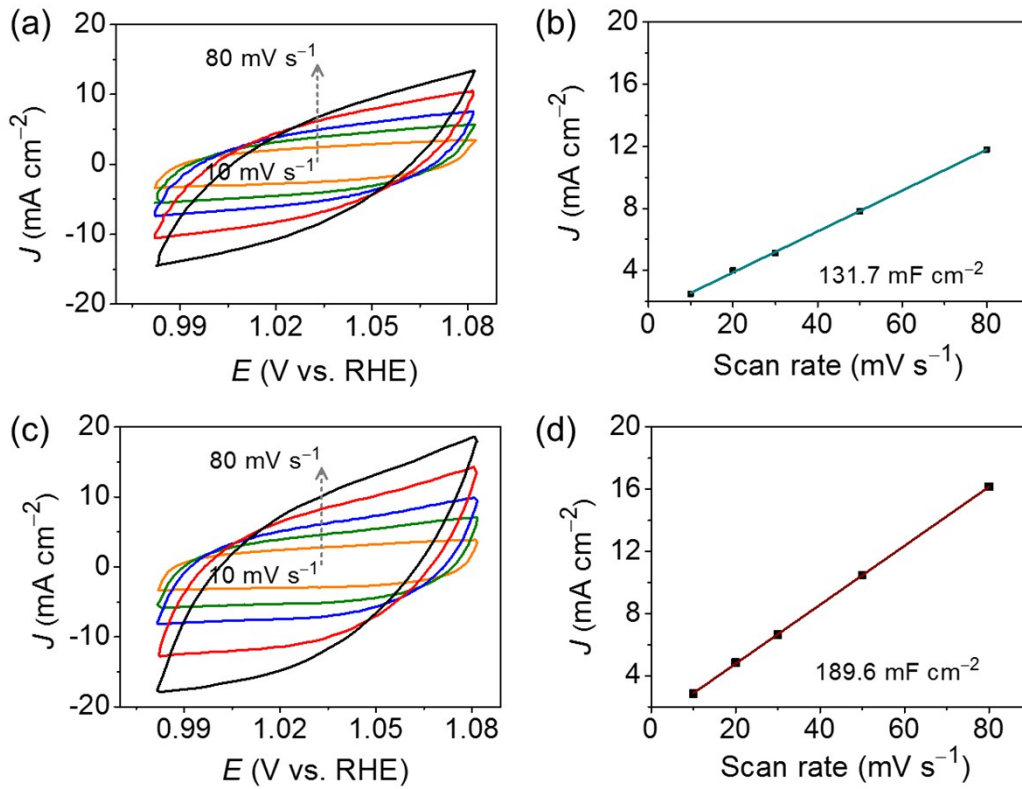


Fig. S25 CV curves and linear fitting curves of the capacitive currents for (a,b) CoO/CC and (c,d) activated F-CoO/CC between 0.98 and 1.08 V at 10, 20, 50, 100, and 200 mV s^{-1} .

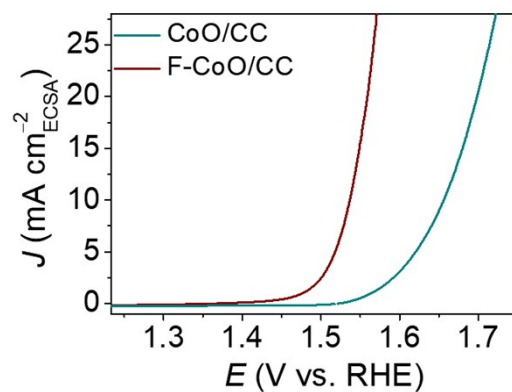


Fig. S26 The OER specific activity normalized to ECSA.

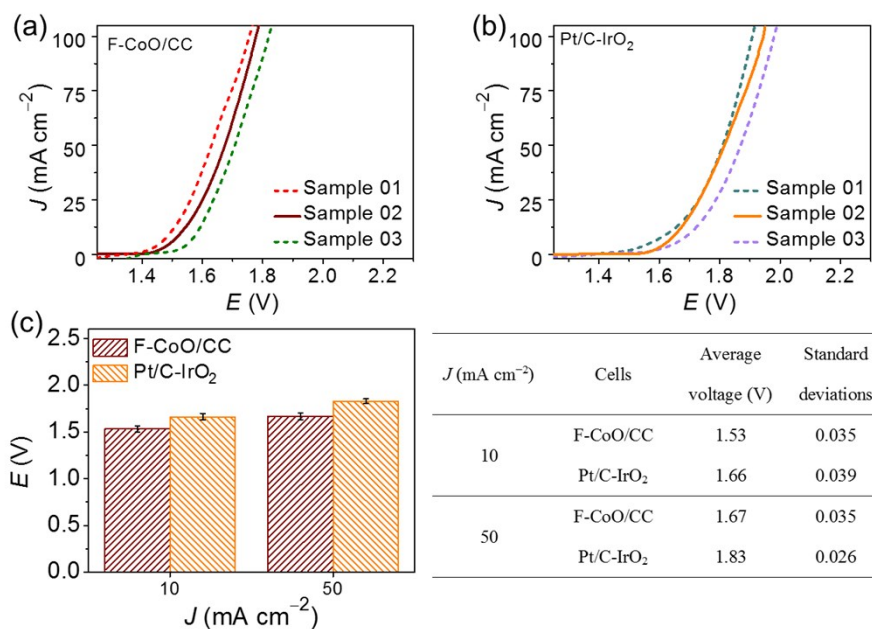


Fig. S27 LSV curves of different (a) F-CoO/CC and (b) Pt/C-IrO₂ cells for overall water splitting. (c) The corresponding average cell voltages of F-CoO/CC and Pt/C-IrO₂ cells at 10 and 50 mA cm⁻² current density. The error bars represent the standard deviations. The overall water splitting performance of these cells is reproducible.

Table S1 F contents of the samples in Fig. S9 measured by XPS.

Samples	Atomic Percentage (at %)			F contents (at %)
	Co	O	F	F/Co
1	31.46	67.13	1.41	4.49
2	36.18	61.32	2.50	6.91
3	37.51	59.22	3.27	8.72

Table S2 Comparison of the electrocatalytic HER activity of previously reported catalysts.

Catalyst	η @-10 mA cm ⁻²	Reference
	(mV)	
F-CoO	53	<i>This work</i>
Co-NiS ₂	80	<i>Angew. Chem. Int. Ed. 2019,</i> <i>DOI:10.1002/anie.201911470.</i>
L-Ag	147	<i>Nat. Catal. 2019, 2, 1107-1114</i>
MoP@NCHSSs-900	92	<i>Angew. Chem. Int. Ed. 2019,</i> <i>DOI:10.1002/anie.201911470</i>
(N, PO ₄ ³⁻)MoS ₂ /VG	85	<i>Angew. Chem. Int. Ed. 2019,</i> <i>DOI:10.1002/anie.201909698.</i>
ANi-PtNWs	70	<i>Nat. Catal. 2019, 2, 495-503</i>
A-CFC	71	<i>Nat. Commun. 2019, 10, 2281.</i>
FeS nanosheets	142	<i>Nat. Commun. 2019, 10, 399.</i>
NCNi/SWCNT70	190	<i>Adv. Sci. 2019, 6, 1802177.</i>
Ni-Fe LDH@NiCu	66	<i>Adv. Mater. 2019, 31, 1806769.</i>
SWCNTs/MoSe ₂ -2:Mo ₂ C	89	<i>ACS nano 2019, 13, 3162-3176.</i>

Table S3 The average Bader charges of the CoO and F-CoO.

Sample	Sites	Bader charge
CoO	Co	7.66
F-CoO	Co	7.80

Table S4 Gibbs free energy of hydrogen adsorption at various sites in (100) and (111) planes.

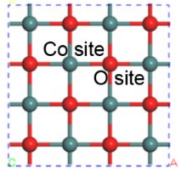
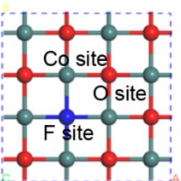
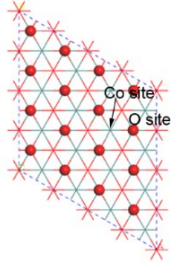
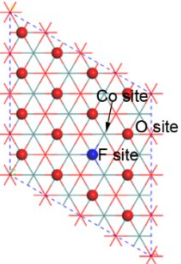
Surface	Models	Sites	ΔG_{H^*} (eV)
CoO (100)		Co	-0.58
		O	0.72
F-CoO (100)		Co	-0.45
		O	0.49
		F	0.75
CoO (111)		Co	1.57
		O	1.36
F-CoO (111)		Co	1.49
		O	0.96
		F	0.85

Table S5 Comparison of the electrocatalytic OER activity of previously reported catalysts.

Catalyst	η @10 mA cm ⁻²	Reference
	(mV)	
Activated F-CoO/CC	237	<i>This work</i>
S NiNx-PC/EG	277	<i>Nat. Commun. 2019, 10,1392.</i>
F-Co ₂ B	320	<i>Energy Environ. Sci. 2019,</i>

		DOI:10.1039/C9EE00950G.
Pt-NC/ Ni-MOF	292	<i>Chem</i> , 2019, 5, 2429-2441.
PBA-60	283	<i>Nat. Commun.</i> 2019, 10, 2799.
IFONFs-45	257	<i>Nat. Commun.</i> 2018, 9, 1809.
w-Ni(OH) ₂	237	<i>Nat. Commun.</i> 2019, 10, 2149.
LSC&MoSe ₂	onset potential 287	<i>Nat. Commun.</i> 2019, 10, 1723.
Bi ₅ CoTi ₃ O ₁₅	320	<i>Nat. Commun.</i> 2019, 10, 1409.
Mn-NG	337	<i>Nat. Cat.</i> 2018, 1, 870.
NiCo ₂ N	289	<i>Adv. Mater. Interfaces</i> 2019, 1900960.
NiCo ₂ S ₄ @g-C ₃ N ₄ CNT-CNT	330	<i>Adv. Mater.</i> 2019, 31, 1808281.
Co/CNFs (1000)	320	<i>Adv. Mater.</i> 2019, 31, 1808043.
CoSe _{2-x} -Pt	255	<i>Adv. Mater.</i> 2019, 31, 1805581.
Co ₃ O ₄ /CeO ₂	270	<i>Adv. Mater.</i> 2019, 1900062.
Ir1@Co/NC	260	<i>Angew. Chem. Int. Ed.</i> 2019, 58, 11868.

Table S6. Comparison of the overall water splitting performance of recently reported electrocatalysts.

Catalyst	Potential @10 mA cm ⁻² (V)	Reference
F-CoO/CC	1.53	<i>This work</i>
Ir1@Co/NC	1.60	<i>Angew. Chem. Int. Ed.</i> 2019, 58, 11868.
NCNi//SWCNT-700	1.57	<i>Adv. Sci.</i> 2019,6, 1802177
(Co _{1-x} Ni _x)(S _{1-y} Py) ₂ /G	1.65	<i>Adv. Energy Mater.</i> 2018, 33, 1802319.
NFN-MOF/NF	1.56	<i>Adv. Energy Mater.</i> 2018, 8, 1801065.
Pt-CoS ₂ /CC	1.55	<i>Adv. Energy Mater.</i> 2018, 1800935.
Rh/SWNTs	1.59	<i>ACS Catal.</i> 2018, 8, 8092–8099.
Co ₃ O ₄ -MTA	1.63	<i>Angew. Chem. Int. Ed.</i> 2016, 55, 1–6.
c-CoSe ₂ /CC	1.63	<i>Adv. Mater.</i> 2016, 28, 7527–7532.
NixCo _{3-x} O ₄	1.75	<i>ACS Appl. Mater. Interfaces</i> 2016, 8, 4718–4723.
NiCo ₂ O ₄	1.65	<i>Angew. Chem. Int. Ed.</i> 2016, 55, 6290–6294.

References

1. Z. L. Wang, X. F. Hao, Z. Jiang, X. P. Sun, D. Xu, J. Wang, H. X. Zhong, F. L. Meng and X. B. Zhang, *J. Am. Chem. Soc.*, 2015, **137**, 15070–15073.
2. J. Kibsgaard and T. F. Jaramillo, *Angew. Chem. Int. Ed.*, 2014, **53**, 14433–14437.
3. J. Kibsgaard, Z. Chen, B. N. Reinecke and T. F. Jaramillo, *Nat. Mater.*, 2012, **11**, 963–969.
4. J. D. Benck, Z. Chen, L. Y. Kuritzky, A. J. Forman and T. F. Jaramillo, *ACS Catal.*, 2012, **2**, 1916–1923.
5. T. R. Hellstern, J. D. Benck, J. Kibsgaard, C. Hahn and T. F. Jaramillo, *Adv. Energy Mater.*, 2016, **6**, 1501758.
6. K. Jiang, B. Liu, M. Luo, S. Ning, M. Peng, Y. Zhao, Y. R. Lu, T. S. Chan, F. M. F. de Groot and Y. Tan, *Nat. Commun.*, 2019, **10**, 1743.
7. J. Kibsgaard, C. Tsai, K. Chan, J. D. Benck, J. K. Nørskov, F. Abild-Pedersen and T. F. Jaramillo, *Energy Environ. Sci.*, 2015, **8**, 3022–3029.
8. G. Kresse and D. Joubert, *Phys. Rev. B*, 1999, **59**, 1758.
9. G. Kresse and J. Furthmüller, *Phys. Rev. B*, 1996, **54**, 11169.
10. G. Kresse and J. Furthmüller, *Comput. Mater. Sci.*, 1996, **6**, 15–50.
11. L. B. Hansen and J. K. Nørskov, *Phys. Rev. B*, 1999, **59**, 7413–7421.
12. J. P. Perdew, K. Burke and M. Ernzerhof, *Phys. Rev. Lett.*, 1996, **77**, 3865.
13. J. Klimeš, D. R. Bowler and A. Michaelides, *Phys. Rev. B*, 2011, **83**, 195131.
14. J. Klimes, D. R. Bowler and A. Michaelides, *J. Phys.: Condens. Matter*, 2010, **22**, 022201.
15. W. Tang, E. Sanville and G. Henkelman, *J. Phys.: Condens. Matter*, 2009, **21**, 084204.
16. G. Henkelman, B. P. Uberuaga and H. Jónsson, *J. Chem. Phys.*, 2000, **113**, 9901–9904.
17. Y. Luo, L. Tang, U. Khan, Q. Yu, H. M. Cheng, X. Zou and B. Liu, *Nat. Commun.*, 2019, **10**, 269.
18. X. F. Lu, L. Yu and X. W. D. Lou., *Sci. Adv.*, 2019, **6**, 1900576.
19. J. K. Nørskov, T. Bligaard, A. Logadottir, J. R. Kitchin, J. G. Chen, S. Pandelo and U. Stimming, *J. Electrochem. Soc.*, 2005, **152**, J23–J26.